pp 54–72. © Royal Aeronautical Society 2016
doi: 10.1017/aer.2016.113

A morphing aerofoil with highly controllable aerodynamic performance

R. Wu
School of Mechanical, Aerospace and Civil Engineering
University of Manchester
UK

C. Soutis
costas.soutis@manchester.ac.uk
Aerospace Research Institute
University of Manchester
UK

S. Zhong and A. Filippone
School of Mechanical, Aerospace and Civil Engineering
University of Manchester
UK

ABSTRACT

In this paper, a morphing carbon fibre composite aerofoil concept with an active trailing edge is proposed. This aerofoil features of camber morphing with multiple degrees of freedom. The shape morphing is enabled by an innovative structure driven by an electrical actuation system that uses linear ultrasonic motors (LUSM) with compliant runners, enabling full control of multiple degrees of freedom. The compliant runners also serve as structural components that carry the aerodynamic load and maintain a smooth skin curvature. The morphing structure with compliant truss is shown to exhibit a satisfactory flexibility and loading capacity in both numerical simulations and static loading tests. This design is capable of providing a pitching moment control independent of lift and higher L/D ratios within a wider angle-of-attack range. Such multiple morphing configurations could expand the flight envelope of future unmanned aerial vehicles. A small prototype is built to illustrate the concept, but as no off-the-shelf LUSMs can be integrated into this benchtop model, two servos are employed as actuators, providing two controlled degrees of freedom.

Keywords: morphing; adaptive aerofoil; multiple degrees of freedom; linear ultrasonic motor

Received 21 December 2015; revised 21 June 2016; accepted 25 September 2016; first published online 17 November 2016.

https://doi.org/10.1017/aer.2016.113 Published online by Cambridge University Press

NOMENCLATURE

C_D	drag coefficient
C_L	lift coefficient
$C_{L\max}$	maximum lift coefficient
C_M	pitching moment coefficient
C_P	pressure coefficient
CFRP	carbon fibre reinforced plastic
LUSM	linear ultrasonic motor
FE	finite element
SMA	shape memory alloy
MFC	microfibre composite
USM	ultrasonic motor
x	location along chord from leading edge

1.0 INTRODUCTION

In order to facilitate take-off and landing and accomplish various manoeuvres, the aerodynamic forces on the wings of a flying vehicle need to be adjusted. This can be achieved by changing the camber of the wing. Conventionally, wing camber is changed using hinged control surfaces, which lead to high local surface curvature, where the flow tends to separate and causes an excessive drag. Therefore, large hinged control surfaces such as flaps are not likely to be used on a regular basis, and this imposes constraints on the size of flight regime of the vehicle.

Wing morphing, which enables changes in aerofoil geometry while maintaining a continuous and smooth aerodynamic surface, has the potential to improve aircraft performance[1-3]. Among various morphing design concepts, a continuous change in camber provides a way of improving aircraft fuel efficiency and mission capability[1,4,5]. Wind-tunnel tests have shown that by replacing a hinged flap with a morphing trailing edge, the L/D (lift/drag) ratio of a 2D aerofoil could be increased by 20–25%[6,7].

The idea of morphing aerofoil was put forwarded in the 1920s and has attracted renewed interest in recent years. However, published aerodynamic data on the performance of morphing aerofoils is still not abundant. Moreover, most researchers have focused on investigating the improvement of aerodynamic efficiency via replacing the hinged flap with a smooth morphing structure. In contrast, the potential of morphing aerofoils to form camber lines with different shapes, which offer multiple morphing strategies (configurations), are often overlooked.

The structural design for a morphing trailing edge is challenging since contradicting requirements such as flexibility, load-carrying capacity and light weight need to be satisfied[8,9]. Nevertheless, a few practical concepts are available. For example, the topology synthesis method can be utilised to design compliant structures that are capable of performing desired morphing under a simple actuation displacement without causing a significant strain while satisfying other design constraints[6,10]. It has been reported that a morphing trailing edge designed by such a method is capable of providing $\pm 10°$ flap deflection, 1°/foot twisting along the span and a satisfactory loading capacity[1-3]. An adaptive "belt rib" concept is designed to replace the conventional ribs. It consists of a closed shell (belt) and in-plane spokes that are hinged to the shell[1,4,5]. Such a structure is naturally flexible and allows

https://doi.org/10.1017/aer.2016.113 Published online by Cambridge University Press

morphing with a single degree of freedom. Meanwhile, studies have shown that boundary layer can be stabilised to delay flow separation by replacing a wing's rigid upper skin in front of the conventional hinged aileron by an adaptive composite skin that is actuated along the out-of-plane direction[11-13]. An array of actuators beneath the skin is used to deform the skin into different shapes optimised for various flight conditions. Similar structures can also be used on other parts of the wing and to achieve drag reduction[14-16].

Selection of a morphing actuator that is lightweight, small in size, power-efficient and fail-safe is another challenge. A smart material actuator that can directly convert electrical, magnetic or thermal stimulation to mechanical displacement is believed to offer a way to satisfy some of these requirements[7,17]. The most widely studied smart materials for actuation include shape memory alloys (SMA) and piezoelectric ceramics. However, SMA has a limited maximum strain of 8%, and its two-way shape memory effect fades out as it cycles[8,9]. Also, although SMA can be fast-reacting, the speed of activation and deactivation relies on the heating rate and cooling conditions, which impose a barrier to high-frequency operation[6,10]. Furthermore, their power consumption can be increased significantly as a result of cooling[18]. Piezoelectric ceramic can output large force at high speed and frequencies, and it has a power density 100 times that of SMA[19]. Although the maximum strain of piezoelectric ceramic is only ~0.1%, they are usually used as microfibre composite (MFC) to bend thin structures[2], and they can be an attractive option if the actuation displacement could be amplified without sacrificing the actuation force.

In this paper, a new morphing design concept is presented and it is applied to an asymmetrical aerofoil (NACA 4418). A compliant truss structure that has multiple truss elements hinged to a compliant upper skin forms the morphing structure. The actuators between truss elements are controlled independently to allow continuous camber change with multiple degrees of freedom. A linear ultrasonic motor based on piezoelectric ceramics is proposed as the morphing actuator, and it can potentially provide unlimited linear output while retaining the high actuation force. It also copes well with the challenge of morphing since the runners can be compliant and multifunctional to serve as the structural components. Our numerical simulations and wind-tunnel tests show that besides the widely recognised benefits of a morphing aerofoil over hinged control surfaces, the vehicle flight regime can be further extended by switching between different morphing strategies and allowing the pitching moment control independent of C_l.

2.0 THE PROPOSED MORPHING AEROFOIL CONCEPT

2.1 Linear Ultrasonic Motor (LUSM)

In a typical LUSM, pieces of piezoelectric ceramics are used to generate vibration at ultrasonic frequencies and form a travelling wave. The travelling wave can drive a body in contact with the ceramics through friction; therefore, the high-frequency displacement from the piezoelectric ceramics can be converted into a constant linear velocity. In this way, the limited actuation displacement of the piezoelectric ceramics is amplified to a theoretical infinite without necessarily sacrificing actuation, making a competitive morphing actuator possible. Also, when the LUSM is powered down, the piezoelectric ceramics could inherently hold the runner and provide blocking force, which makes it fail-safe. However, LUSM is rarely reported being used in morphing structures.

In Table 1, three off-the-shelf LUSMs are set in comparison with revolving ultrasonic motors (USM) and electric motors that have been reported in literature[20]. In terms of power

https://doi.org/10.1017/aer.2016.113 Published online by Cambridge University Press

Table 1
Actuator comparisons[20]

Actuator	Output force/torque	Holding force	Velocity	Weight (g)	Power density (W/kg)
N216 NEXTLINE® (LUSM)	60 kg	80 kg	1 mm/s	1,250	0.48
N422 Linear Actuator (LUSM)	0.7 kg	1 kg	5 mm/s	25	1.4
U-264 RodDrive OEM (LUSM)	0.3 kg	1.5 kg	200 mm/s	80	7.5
SPL-801 (USM)[20]	10 kg·cm	N/A	210 rpm	249	95
Maxon DC motor (brushless)[20]	0.076 kg·cm	-	25,000 rpm	86	235
Harmonic gear with DC motor[20]	32 kg cm	N/A	60 rpm	739	27

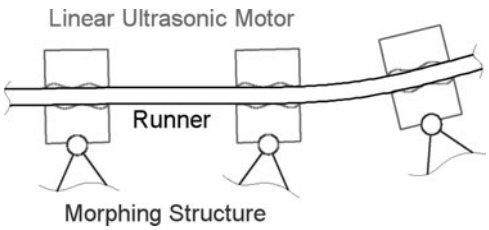


Figure 1. Schematic view of the actuation system concept with a compliant runner and LUSMs, where LUSMs are pivoted onto the actuated morphing structure and the runner naturally forms a smooth curvature.

density, which is a critical parameter for morphing actuators, LUSM is not attractive. However, the main reason for this drawback is that LUSM is currently developed as a positioning device due to its intrinsic fast response and high open-loop precision, rather than as a heavy-duty actuator. There is a significant room for further improvements, such as in weight reduction and power enhancement. It has been reported that the power of ultrasonic motors could be increased for instance by fine-tuning the driver frequency[19,20].

Meanwhile, DC motors usually need a transmission mechanism to reduce the speed, which significantly decreases power density. For example, the power density of DC motor in Table 1 is reduced from 235 W/kg to 27 W/kg when a harmonic gear transmission system is used[20]. This will also lead to an increased space occupation and a reduced reliability.

Therefore, LUSM has the potential to be a future morphing actuator solution, especially when space is strictly limited, such as in miniature unmanned aerial vehicles (MUAV), or when a large number of actuators is needed to control numerous degrees of freedom.

2.2 The proposed concept: compliant runners driven by LUSM

The LUSM requires a compliant runner that can provide effective contact with the piezoelectric actuator. Keeping this in mind, an actuation system with multifunctional compliant runners driven by LUSMs is proposed, as shown in Fig. 1. Since a homogeneous

https://doi.org/10.1017/aer.2016.113 Published online by Cambridge University Press

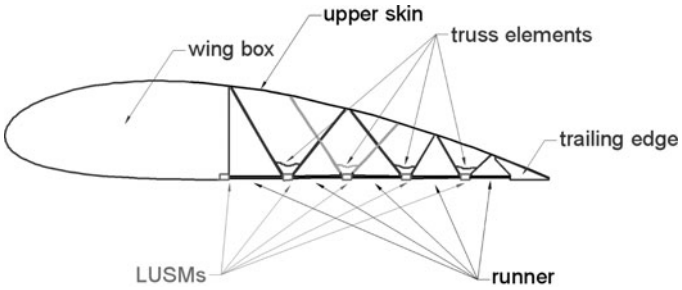


Figure 2. Schematic view of the morphing aerofoil concept with the compliant truss configuration and the proposed LUSM actuation system. The system provides five degrees of freedom.

compliant runner naturally maintains a smooth curvature under bending and is able to provide out-of-plane stiffness and axial stability, it is an ideal actuator for a morphing wing in which a smooth aerodynamic surface, structural compliance and loading capacity are required.

As shown in Fig. 1, multiple LUSMs pivoted to a morphing structure with multiple degrees of freedom could run along the same runner. Therefore, all the degrees of freedom can be controlled and a smooth curvature can be formed. Such an actuation system can be integrated into various morphing structures as a universal actuator solution.

When used on the surface of a morphing wing, it is necessary for it to be airtight. This can be achieved by applying morphing skins, such as segmented compliant panels or elastomers, which can passively slide along the runner.

Also, besides the actuation and the structural capacity, more functionality can potentially be embedded into the runner due to its unique position. For example, sensors such as optical fibres can be used to monitor the curvature of the runner, and electronics can be embedded in the runner, thus converting it into a data link between the controller and a large number of actuators.

2.3 The morphing structure

In the morphing aerofoil, the actuation system needs to be supported by a morphing structure that can change shape under actuation, provide loading capacity by eliminating the unwanted degrees of freedom and form the aerodynamic profile. In this research, the baseline NACA 4418 aerofoil was selected because of its relatively high thickness and near-flat lower surface, which makes it easier to manufacture and implement the morphing actuation system.

A carbon fibre composite morphing structure with compliant truss is proposed. As shown in Fig. 2, the morphing aerofoil consists of a rigid wing box (which ends at 40% chord), a flexible upper skin, four independent compliant truss elements and a rigid trailing edge. The actuation system is used as the lower skin of the aerofoil. The LUSMs are positioned at the bottom apex of truss elements, which are hinged to the upper skin. One or more runners are fixed to the trailing edge and slide through the LUSMs as described in Section 2.2. The truss elements shown in Fig. 2 have a span-wise shift to prevent interference with neighbouring trusses with a lower vertex angle between trusses of 60°. This is a compromise between overall structural stiffness and the number of truss elements; it also reduces the thickness mismatch between the rigid wing box and the morphing section under large deflection. The number of actuators is equal to the number of truss elements, spaced equally along the runner.

https://doi.org/10.1017/aer.2016.113 Published online by Cambridge University Press

When the truss elements are sliding along the runner, the morphing structure will bend or straighten and the camber of the aerofoil will change. During morphing, the flexible composite upper skin and the runners on the lower skin will maintain smooth curvature that guarantees aerodynamic efficiency. The truss elements will also undergo small elastic deformation that can be accommodated by their compliance.

A major advantage of this morphing structure is that it can morph with multiple degrees of freedom and thus provides a wide range of camber line shapes, which is enabled by the independent actuation of the four truss elements as well as the rigid trailing edge by the five sets of LUSMs. Meanwhile, the CFRP truss structure naturally possesses high specific stiffness and strength, and provides adequate loading capacity. For the same reason, low bending stiffness of the structural elements is allowed, which leads to low resistance to camber morphing.

2.4 Simulation of Morphing Process

A nonlinear FE simulation is carried out to show the morphing process of the proposed aerofoil and to assist later analysis.

A 3D model of the morphing aerofoil is constructed with a 280 mm chord and 5 mm span. All materials are assumed to be linear, elastic and isotropic. The upper carbon fibre reinforced plastic (CFRP) skin is 0.25 mm thick ($E = 100\,GPa$, $\rho = 1.6\,g/cm^3$), the trusses are made of 0.5 mm thick CFRP plate, the lower joints of trusses are plywood ($E = 800\,MPa$, $\rho = 0.7\,g/cm^3$), the runners are CFRP rods of 1 mm diameter ($E = 100\,GPa$, $\rho = 1.6\,g/cm^3$), and the LUSM are replaced by CFRP plates. The lower morphing skin is not included since it should not have significant effect on the morphing process. The model has the same material properties and dimensions to the prototypes discussed in Section 5, except that it is a near 2D model with a 5 mm span and only one runner is included.

In the analysis, the hinges between the truss and upper skin are assumed to provide no bending resistance. Sections of runners are fixed between adjacent actuators, and actuation is represented by thermal contraction/expansion of the runners. This does not resemble the interface between the piezoelectric ceramic and the runner, but it fully replicates the conditions of the morphing structure under actuation (while ignoring small change of the runner's diameter) and significantly saves computational time. The thermal contraction of different sections of runners can be controlled independently, so all five degrees of freedom can be manipulated.

The structural weight (excluding the wing box) from the simulation is 22 grams, which is equivalent to 440 grams per meter span, and the morphed shape, as shown in Fig. 3, is smooth. However, slight waviness can be seen in the upper and lower skins, which is captured in both the analysis models and wind-tunnel test models. According to the literature[21], lift and drag are barely influenced by an upper surface protuberance located after the middle chord with a height of up to 0.5% of chord length; thus, this waviness is expected to have a minor effect on the morphed aerofoil's performance. More morphing configurations are shown in Section 3.

2.5 Numerical simulation of loading capacity

Achieving sufficient load carrying capacity is an additional objective of morphing aerofoil design. As a preliminary assessment, a nonlinear static FE simulation is carried out to test the model aerofoil's loading capacity.

The model has the same material properties and dimensions to the one used in Section 2.4, except that the span is 50 mm, and 10 rods with 5 mm spacing are included, making it

https://doi.org/10.1017/aer.2016.113 Published online by Cambridge University Press

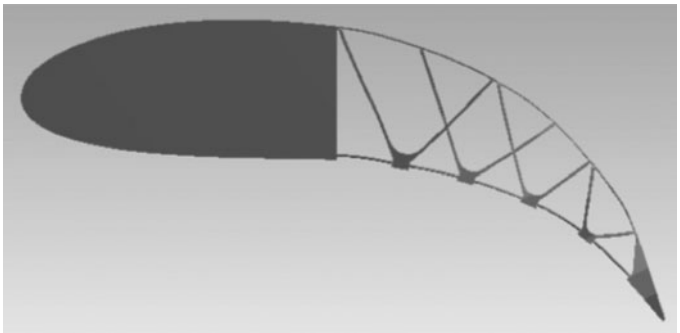


Figure 3. Finite-element simulation illustrating a morphing configuration with near-maximum trailing-edge deflection.

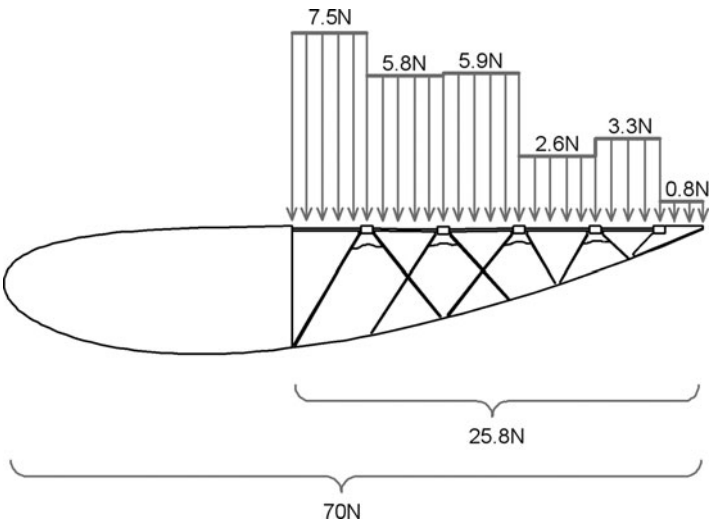


Figure 4. Chord-wise load distribution used in the static load simulation with an overall load of 70 N.

identical to the static prototype discussed in Section 5. The aerodynamic load is assessed with the 2D Xfoil code (see Section 3), then the load distribution on both sides of the aerofoil is integrated into six forces evenly distributed within 6 adjacent regions on the lower surface of the morphing part, and then the forces are applied to the same regions of the 3D structural model. The six regions are divided by the actuators and trailing edge, as shown by Fig. 4. This loading condition is identical to the static loading test on the prototype built in Section 4. There is no direct load on the upper surface since the aim here is to evaluate the load-carrying capacity of the truss structure, while the behaviour of the upper skin can be modified as needed if bigger models were constructed; the objective is to illustrate the morphing concept and demonstrate it in a small physical model.

Three different loading conditions with the whole aerofoil carrying 70 N, 130 N and 250 N load are simulated. No large deformation is observed, and the results are listed in Table 2, where both the maximum deflection across the aerofoil and the deflection of trailing edge are reported, and the ratio of maximum deflection in chord length is also reported to show the extent of deformation. Three equivalent flight conditions are included in Table 2 to provide

https://doi.org/10.1017/aer.2016.113 Published online by Cambridge University Press

Table 2
Results of the static structural simulation

Load (N)	Deflection (mm)	Def./chord	Equivalent condition	Note
70	0.36 (0.2 at TE)	0.13%	$C_l = 0.8$, v = 80 m/s, SF = 1.5	Baseline AoA = 3.6°
130	0.56 (0.3 at TE)	0.2%	$C_l = 1.5$, v = 80 m/s, SF = 1.5	Baseline max. lift
250	1.17 (0.5 at TE)	0.42%	$C_l = 1.5$, v = 111 m/s, SF = 1.5	Baseline max. lift

SF = safety factor, which is applied to force; TE = trailing edge; AoA = angle-of-attack.

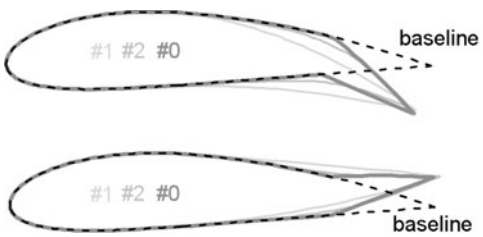


Figure 5. 2D aerofoil models at 0° angle-of-attack with three different morphing strategies.

an idea about the possible flight regime. It should be noted that the load here represents the overall load across the whole aerofoil, and the morphing part only carries 26 N, 48 N and 93 N loads respectively, since most of the aerodynamic force is generated near the leading edge.

3.0 AERODYNAMIC PERFORMANCE

Unlike conventional hinged flaps, the morphing aerofoil always maintains a smooth surface, and it can be controlled with multiple degrees of freedom. In order to investigate the aerodynamic impact of these features, aerodynamic analysis and wind-tunnel tests are carried out to evaluate the performance of the aerofoil (with a baseline profile of NACA 4418) at different morphing configurations and flight conditions (different angles of attack).

3.1 Morphing strategies

The multiple degrees of freedom of the proposed morphing aerofoil can be used to generate different morphing configurations. This can be done by controlling the five sets of LUSMs independently in reality, or assigning the thermal expansion of the five rods independently in the structural simulation, as discussed in Section 2.4.

The morphing leads to camber change, and multiple actuators along the chord can alter the curvature of the camber line at different chord-wise locations. At a constant trailing-edge deflection, different morphing settings yield aerofoils with different camber line shapes (Fig. 5). There is an infinite number of possible morphing shapes; for an aerofoil with camber increased at one location, that location can be continuously moved along the chord by adjusting the output of different sets of actuators. As shown in Fig. 5, two intuitively defined morphing strategies and a conventional hinged flap are considered:

https://doi.org/10.1017/aer.2016.113 Published online by Cambridge University Press

- Strategy 1: Morphing aerofoil with camber intensively changed near the maximum thickness and an unchanged trailing edge
- Strategy 2: Morphing aerofoil with camber intensively changed near trailing edge
- Strategy 0: Aerofoil with a hinged flap at 0.75 chord length.

The 2D aerofoils shapes for aerodynamic analysis are generated using the 3D models resulting from the structural simulations. In the structural simulations, the ratio between the amounts of runner expansion is kept constant for each morphing strategy to realise different trailing-edge deflection with a similar camber line shape.

3.2 Aerodynamic analysis set-up

3.2.1 Xfoil analysis

Xfoil is a code widely used in research to analyse the flow around a subsonic aerofoil. It is based on a revised 2D panel method that takes into account the viscosity and compressibility effects, allowing reasonable predictions of lift, drag and pitching moment, as well as the flow separation point beyond the stall angle[22,23]. In the literature[24], a morphing wing with adaptive upper skin has been tested in wind tunnel at Reynolds numbers similar to those in the present research. The tests use 14–16 pressure taps to measure the pressure distribution on the aerofoil, and the results are then used to determine the location of flow transition. The comparison to Xfoil analysis has shown a close agreement on surface pressure coefficients and transition occurrence.

The computational analysis discussed in the following sections is performed with Xfoil at Reynolds number $Re = 1.5 \cdot 10^6$ (based on the aerofoil chord length) and Mach number $M = 0.235$. This is representative of a 28 cm chord length mini UAV flying at sea level. An analysis with $Re = 0.5 \cdot 10^6$ and $M = 0.078$ is carried out to match the condition of wind tunnel tests.

3.2.2 Wind-tunnel tests

To support the simulations, wind tunnel tests have been performed at a free-stream velocity of 25 m/s and the Reynolds number $Re = 0.5 \cdot 10^6$. Using multiple rigid models, seven different aerofoil morphing states are tested, including: baseline (strategy 0 with 0 mm deflection), strategies 0, 1 and 2 with 30 mm downward and 20 mm upward deflections.

3.2.2.1 Model construction

Rigid models with a 280 mm chord (same as in aerodynamic analysis) and a 600 mm span and cross-sections representing different morphing states are made by laying up glass fibre cloth with epoxy onto a reinforced foam core, forming a skin of ~0.5 mm thickness. The foam core is shaped by a CNC hot-wire cutting machine with the tolerance of around 0.5 mm due to material burn-off. All the models are polished with P180 sandpapers to give a fairly smooth surface finish.

The hinged aerofoil model has a movable flap which is attached to the fore body via three hinges along the span. The flap has a circular leading edge that can just fit into the concave slot in the rare part of the fore body to eliminate all gaps between the fore body and the flap. This ensures the aerofoil surface to be as smooth as possible (with fluctuation height near the junction < 1 mm) and no air can escape from the lower surface to the upper surface.

https://doi.org/10.1017/aer.2016.113 Published online by Cambridge University Press

3.2.2.2 Wind-tunnel set-up

The aerofoil is tested in the Project tunnel at University of Manchester. The tunnel has an octagonal test section measuring 87 cm × 111 cm (height × breadth). To ensure a 2D flow around the aerofoil, the aerofoil model is mounted between the two splitter plates spanning the whole width of the test section. The function of splitter plates is to isolate the tips of aerofoil models from the tunnel wall boundary layers and to ensure a near 2D aerodynamic behaviour. A 2 mm gap is left between the splitter and each end of the aerofoil for clearance. The aerofoil model is mounted to a six-component load balance through a sting, which passes through a hole in the upper splitter plate.

The speed measured at the original test section inlet cannot be used since the complicated blockage effect caused by the splitter plates, test model and tunnel wall will alter the flow velocity between the splitters[25]. The free stream speed is determined instead with a Pitot tube located between the splitters at 11 cm away from the sidewall and 60 cm upstream of the aerofoil leading edge.

The test points are recorded by a computer program that averages the data sampled at 1 kHz during a second. To further reduce the fluctuation, each data points reported in this paper is the average of five repeated tests.

The maximum total blockage effect, including the contribution of solid blockage and wake blockage, is lower than 3.5%. All the test data reported in this paper have been corrected for blockage effect and lift effect, as well as circulation effect that account for a change up to 7% in the measured dynamic pressure due to proximity of the pitot tube to the aerofoil model[25,26].

3.3 Aerodynamic results

3.3.1 Results on aerofoils with an increased camber

Before moving on to a detailed discussion of the result, it is worth explaining the function of the layout of Figs. 7 and 8. Each of these figures has set three subplots in comparison. The subplots represent the results from Xfoil analysis at two different Reynolds numbers and the wind-tunnel test, respectively. Figure 7(a) shows the results at $Re = 1.5 \cdot 10^6$, which is representative of a UAV. The key results can be derived from this figure but still require experimental validation. Figure 7(b) shows the results from the wind-tunnel tests, which are carried out at a lower Reynolds number of $0.5 \cdot 10^6$, due to the constraint of test models and equipment; this included only one deflection due to the time limitation. However, it is sufficient to support the analysis results if the Reynolds number effect is not significant. Therefore, Fig. 7(c) is plotted, which shows the analysis results at the test Reynolds number. By comparing it to Fig. 7(b), it can be seen that the curves from the test and the analysis results show very similar trends despite the difference in magnitudes that is discussed later. The comparison between Fig. 7(c) and Fig. 7(a) shows that the Reynolds number effect has causes no significant change in the trend of the curves. Therefore, the trend of the curves shown by Fig. 7(a) is supported by experimental results (and similar for Fig. 8(a) and for the results discussed in Section 3.3.2), and the key conclusions on the effects of different morphing strategies can be made.

The difference in the results' magnitudes is mostly caused by the way that lift and drag are measured, which includes the test model's 3D effects. In Fig. 6, lift and drag results of the baseline aerofoil NACA 4418 from the wind-tunnel test, Xfoil analysis and NACA Langley wind tunnel[27] are compared. As shown in the figure, the analysis shows good agreement with NACA test results, but the test results in the presented research shows differences. For

https://doi.org/10.1017/aer.2016.113 Published online by Cambridge University Press

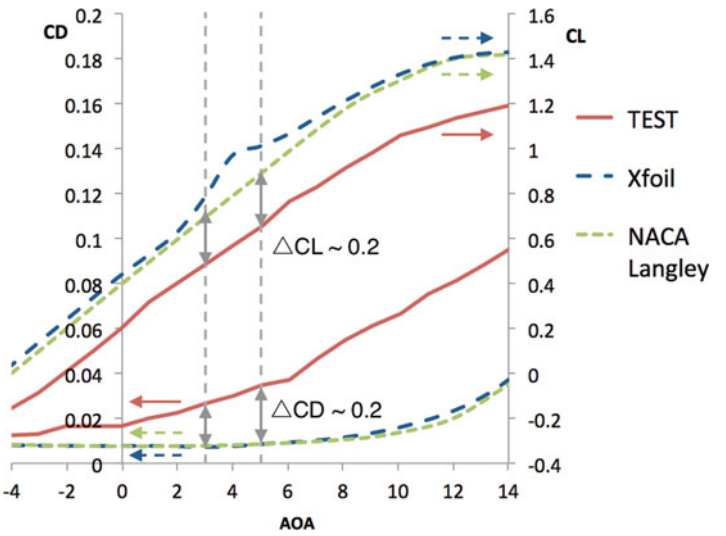


Figure 6. (Colour online) Comparisons between lift and drag coefficient of the baseline NACA 4418 aerofoil from the present wind-tunnel test ($Re = 0.5 \cdot 10^6$), Xfoil analysis ($Re = 0.5 \cdot 10^6$) and NACA Langley wind-tunnel test ($Re = 3 \cdot 10^6$)[27].

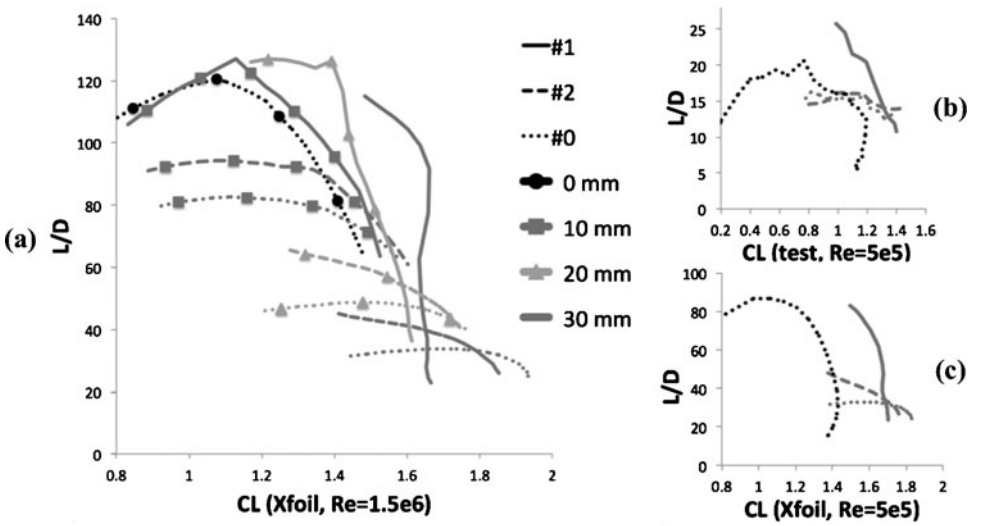


Figure 7. L/D -C_L curves of aerofoils with increased camber and different trailing-edge deflections, showing morphing strategies outperforming hinged aerofoil (dotted lines) and outperforming each other at different C_L range, all aerofoils except the baseline have 0°∼10° angle-of-attack.

instance, within an angle-of-attack range of 3°∼5°, the C_D is approximately 0.02 greater and C_L is around 0.2 lower.

In the NACA test, the lift is deduced from the pressure distributions measured on the aerofoil surfaces, and the drag is evaluated from the pressure in the wake[27]. Such methods allow the measuring devices to be placed near the centre of the wing span[28], and hence the 3D effect can be significantly reduced, whereas in the present wind-tunnel test, all the forces

https://doi.org/10.1017/aer.2016.113 Published online by Cambridge University Press

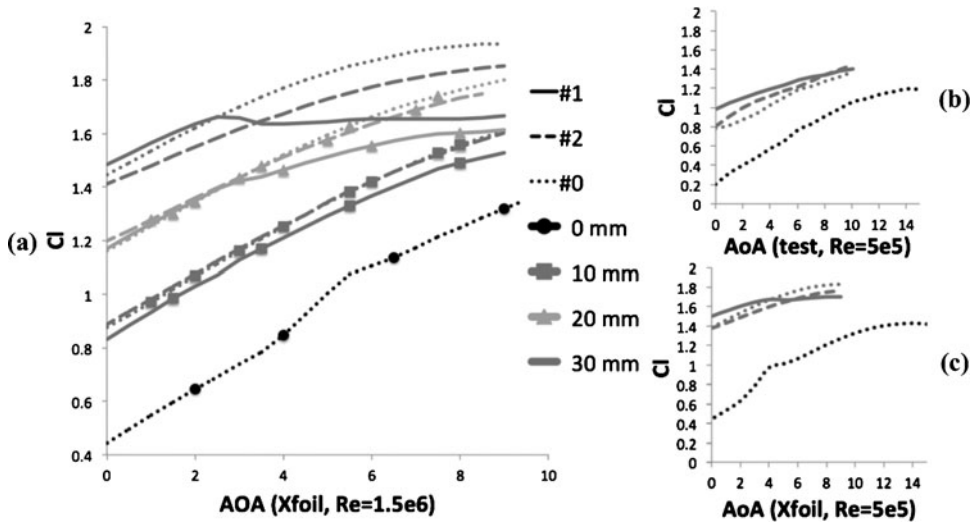


Figure 8. Lift curves of aerofoils with increased camber and different trailing-edge deflections, showing that the strategies with the highest efficiency in Fig. 7 lose lift at relatively low angle-of-attack.

are measured directly with the force balance and the forces on the wing tips are included. The mechanical clearance between the wing tips and splitters causes 3D effects that increase drag and reduce lift that leads to the difference in the results.

To briefly summarise the observations from the results, when the morphing strategy changes from strategy 1 to 2 and finally to strategy 0, which is the aerofoil with a hinged flap, the location of maximum camber increment moves towards the trailing edge and the maximum curvature of the camber line increases. It is shown by the results that when such changes are made, the aerofoil tends to be more efficient (higher L/D) at higher angles of attack and less efficient (lower L/D) at lower angles of attack.

In Fig. 7, L/D ratio is plotted against C_L, which shows that at each trailing-edge deflection, morphing strategy 1 yields the highest L/D ratio among the three configurations within the lower range of C_L tested, but its L/D drops more rapidy than other strategies at higher C_L, which is obviously associated with a rapid increase in C_D. It can be seen in the figure that C_L can be increased by increasing trailing-edge deflection. Morphing strategy 1 is the most efficient until C_L is over ≈1.7 with a maximum trailing-edge delfection of 30 mm. Morphing trategy 2 gives the highest L/D ratio until C_L ≈1.8. At higher C_L values, strategy 0, is the better performing morphing configuration.

As shown in Fig. 8, where C_L is plotted against angle-of-attack, strategy 1 starts to stall and lose lift earlier (at ∼3° angle-of-attack), which suggests that strategy 1 can only be advantageous at low angles of attack. The maximum C_L that can be achieved by the three strategies while keeping C_D below a certain value is presented in Fig. 9. The baseline NACA 4418 is also plotted as a reference without the C_D constraint (C_D varies), It can be seen that as the angle-of-attack increases, or as the maximum attainable lift increases (at the expense of drag), the most efficient strategy changes from strategy 1 to 2, and finally to strategy 0 (hinged flap) when a very low L/D ratio is obtained. It is a sequence in which the location of maximum camber increment approaches the trailing edge and the maximum camber line curvature increases. The curves in Fig. 9 are rather zigzagged since the data

https://doi.org/10.1017/aer.2016.113 Published online by Cambridge University Press

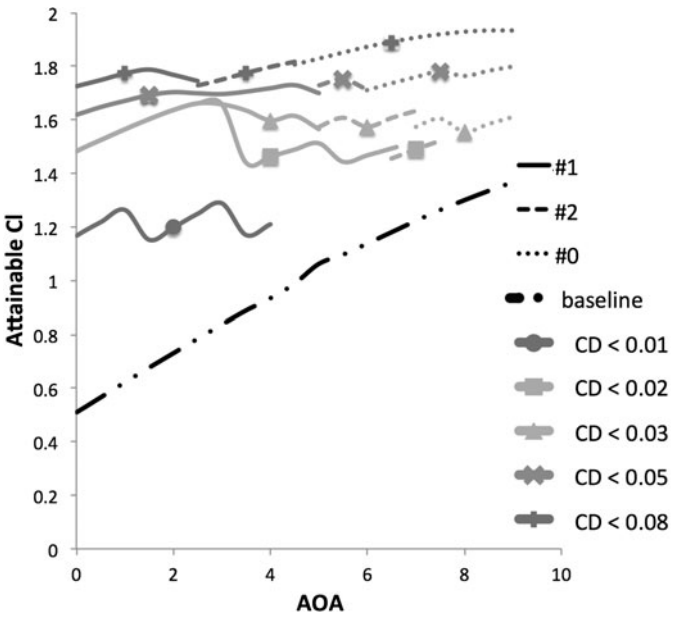


Figure 9. Attainable C_L by three morphing strategies with varied C_D values, generated by Xfoil analysis.

points are generated from discrete data with seven trailing-edge deflection values and three strategies.

The morphing aerofoils outperform the baseline, while the improvements in efficiency over hinged flaps at relatively high angles of attack (see Fig. 9) are not as significant as some previous studies have suggested. This may be because the hinged aerofoil used in the wind-tunnel tests in this research has been made as smooth as possible and the junction between wing and flap has been made airtight.

The reason why strategy 1 is efficient only at low angles of attack and suffers from low $C_{L\max}$, while strategy 0 (the hinged flap) is the most efficient at high angles of attack can be explained in terms of flow separation. Flow separation occurs when the speed of the boundary layer decreases to zero under an adverse pressure gradient. Figure 10 shows the pressure coefficient (C_P) across the aerofoil with unit chord length at 6° angle-of-attack using an inviscid analysis (where the flow always stays attached to show the complete pressure gradient), as well as the separation point predictions from analysis with viscous effect (where the flow separates in the trailing-edge region). Focusing on the region with x $\approx$ 0.6$\sim$0.8 on the upper surface where flow separation starts, strategy 1 (aerofoil with intensively increased camber near the maximum thickness) forms a relatively uniform variation in curvature, and therefore, consistently increasing adverse pressure gradient that the boundary later cannot overcome; thus, the flow separates early in this region and causes excessive drag. Strategy 0 (hinged aerofoil) forms an intensively curved surface near the hinge, where a favourable pressure gradient is formed; thus, the flow accelerates in this region and separation is delayed to the hinged point. The behaviour of strategy 2 (aerofoil with maximum camber increment near trailing edge) is between the other two.

Therefore, the efficiency of different strategies can be explained: although strategy 1 (aerofoil with maximum camber increment near leading edge) is the most efficient at low

https://doi.org/10.1017/aer.2016.113 Published online by Cambridge University Press

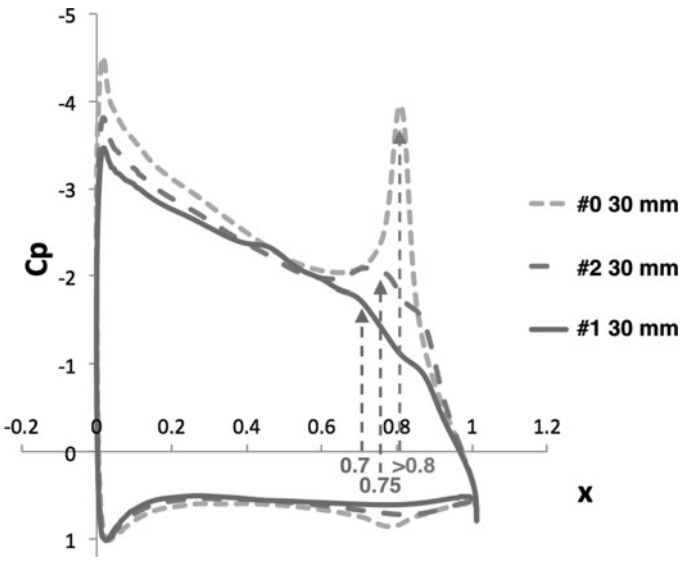


Figure 10. C_P-x (x = location along chord from leading edge) curve of aerofoils with 30 mm downward trailing-edge deflection via different morphing strategies generated by inviscid analysis, and flow separation point predicted by viscous analysis.

angles of attack, when the location of maximum camber increment moves towards trailing edge, the flow separation points also move towards the trailing edge and lead to a higher lift and a lower drag at high angles of attack.

To be noted, the hinge pivot of strategy 0 (hinged aerofoil) is located at 75% chord length, but in Fig. 10 the hinge point is near 80% since the flap is deflected so the horizontal length of the flap is reduced. The three aerofoils have very similar chord length after morphing, and are normalised to unit chord length for illustration.

3.3.2 Results on aerofoils with a decreased camber

Aerofoils with decreased camber can generate low or negative lift for high-speed flight or manoeuvre and control pitching moment coefficients for manoeuvre or trimming.

As discussed in Section 3.3.1, the key conclusions from the analysis are supported by the wind-tunnel tests, so only test data are presented in this section for a clear illustration (see Fig. 11).

Since the reflexion of the camber line near the trailing edge lets these aerofoils generate less or negative lift in the trailing-edge region, the pitching moment C_m is increased and the increment is related to the camber line shape. Therefore, as shown by Fig. 11, strategies 1 and 2 yield different near-zero or positive C_m. Meanwhile, similar to Section 3.3.1, strategies 1 and 2 yield similar C_L since they have the same trailing-edge deflection. Thus it is possible to control pitching moment while maintaining constant C_L by moving the location of maximum camber change towards the trailing edge. However, a drag penalty exists according to the C_D curves, but it is considerably lower than for a hinged flap.

As an example of the pitching moment control independent of C_L, according the C_m curves in Fig. 11, a C_m increment of approximately 0.04 can be induced by changing the morphing strategy from strategy 1 to 2, while the C_L and C_D curves are barely changed.

https://doi.org/10.1017/aer.2016.113 Published online by Cambridge University Press

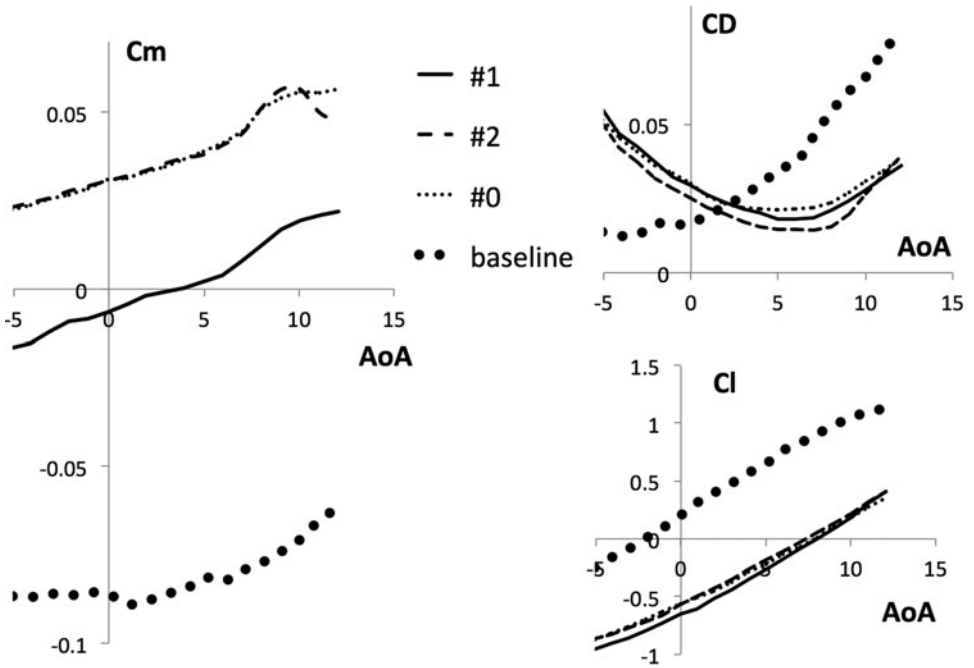


Figure 11. C_m C_D and C_L versus AoA of aerofoils with decreased camber and 20 mm trailing-edge deflections, showing changes in C_m independent of C_l with little penalty in C_D.

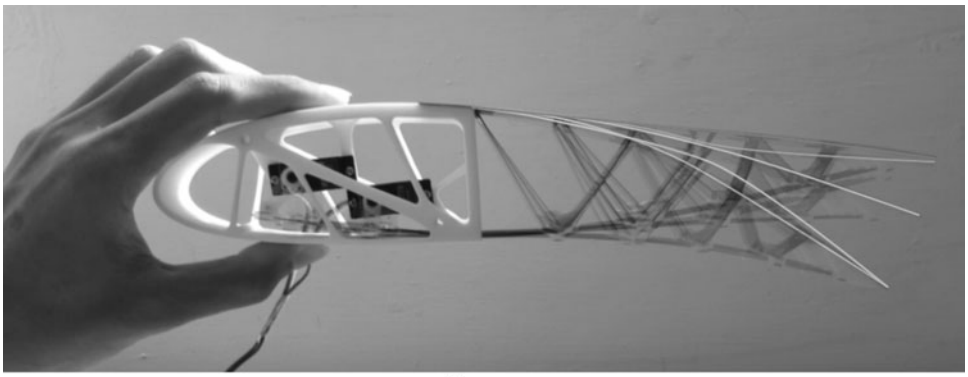
4.0 PROTOTYPING

To further understand the behaviour of the morphing aerofoil, two prototypes are made, including a static prototype aiming to validate the loading capacity and a moveable prototype aiming to test the morphing mechanism.

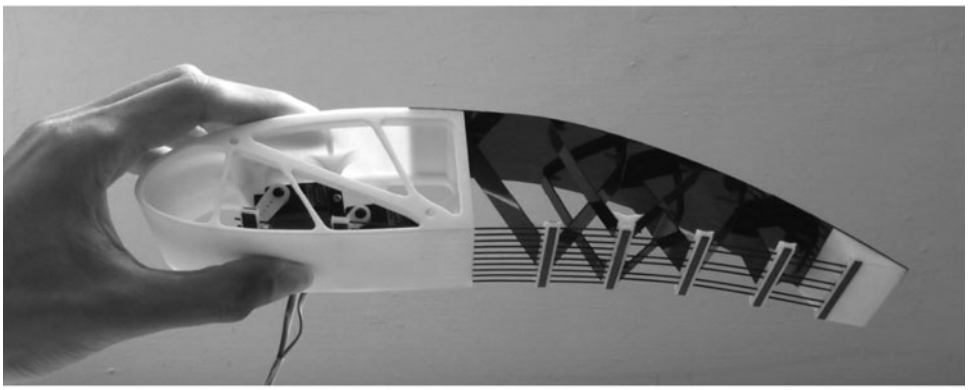
The static prototype is similar to the simulation model, but with some minor differences in materials. 3D printed nylon reinforced by CFRP plates is used in some parts. Since no change is made in the compliant structures including the trusses and the upper skin and runners, which are still made of CFRP, the mechanical behaviour of the prototype should be very similar to the simulation results. In addition, all the hinges are made of composite panel with Kevlar fibre and cyanoacrylate matrix ("super glue"). The matrix along the hinge line is cracked to allow free rotation with negligible rotational resistance, and this is similar to the simulated condition. The prototype also includes a 3D printed wing box, which is overdesigned to sustain the load from the static loading test without inducing perceptible deformation. The finished morphing trailing edge weighs 0.22 N, which is close to the simulation prediction.

The static loading test is carried out with 26 N and 22 N load applied in the way identical to the simulation, which corresponds to the overall load of 70 N and 60 N across the whole aerofoil. The bonding between several hinges and upper skin fails under the load of 70 N. But under the load of 60 N, no failure is observed, and a trailing-edge deflection of 0.2 ± 0.1 mm is induced, which is close to the simulation prediction shown in Table 2. However, the out-of-plane deflection of the upper skin is larger than predicted due to excessive initial deflection induced by manufacturing defects.

https://doi.org/10.1017/aer.2016.113 Published online by Cambridge University Press



(a)



(b)

Figure 12. Moveable prototype. (a) Side view showing five different morphing states. (b) Oblique view showing the runners are connected to either the trailing edge or the second truss from the left.

The moveable prototype (Fig. 12) is similar to the static prototype, but the runner diameter is reduced from 1 mm to 0.8 mm to reduce the bending stiffness and therefore the resistance to morphing. The trailing edge and the second truss from the leading edge are each driven by one digital servo through five runners. Those runners slide through the lower joint of the truss elements while having one end fixed to the truss that is driven by it and the other end connected to a servo. Thus, the conditions are equivalent to a LUSM driven structure and the only difference is the actuators' location. According to simple analysis, it will provide the same actuation capacity (it could support 250 N overall static load while inducing <1 mm out-of-plane deflection) and 40% of the out-of-plane loading capacity in comparison with the static prototype, while the bending resistance of rods is also reduced to 40%.

As no off-the-shelf LUSMs can be integrated into this small demonstrator, servos are used instead of LUSMs. This also provides a practical way to drive the presented morphing structure using conventional actuators before the development of LUSM could offer a viable solution. The moveable prototype has two servos as actuators, and therefore two controlled degrees of freedom. The servos are controlled by two PWM signals generated from a STC80C516RD microcontroller. The morphed shapes are shown in Fig. 12.

It should be noted that at this stage, neither prototypes has morphing skin on the lower surface. This will not have a significant influence on the tests since the skin has a minor effect

https://doi.org/10.1017/aer.2016.113 Published online by Cambridge University Press

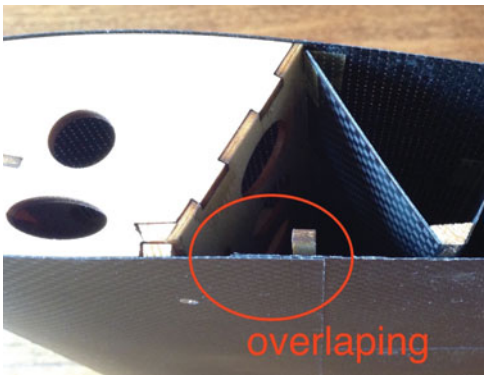


Figure 13. (Colour online) An example of an overlapping segmented bottom morphing skin that can be utilised to form an airtight aerofoil and transfer the aerodynamic load.

on morphing or strength. The morphing skin will affect the flow and will require further examination in the near future. As an example, the segmented morphing lower skin shown in Fig. 13 could be introduced; it consists of two overlapping skins that are bonded to the rigid wing box and the trailing edge, respectively. The rear skin bonded to the trailing edge can slide along the runners and above the skin part that is attached to the wing box.

5.0 CONCLUSIONS

In this paper, a new morphing aerofoil design concept, which combines compliant runners driven by linear ultrasonic motors (LUSMs) with an innovative morphing structure with compliant composite truss, is presented. It is shown to offer fully controlled multiple degrees of freedoms that provide multiple morphing configurations. The compliant truss structure has shown satisfactory specific loading capacity in both static finite element simulation and actual static loading test. The prototype morphing trailing-edge section with a 50 mm span, a 160 mm chord-wise length and a 0.22 N weight can support a 22 N load with a trailing-edge deflection of 0.2 mm.

To validate the aerodynamic benefit of multiple degrees of freedom, the aerodynamic analysis is compared with the wind-tunnel test data. It is demonstrated that when the aerofoil camber is increased, all morphing states show a higher L/D ratio than a conventional hinged control surface at most flight conditions except at very high angles of attack. It is also shown that different morphing strategies outperform the others at different angles of attack. For example, at high angles of attack, the aerofoil aerodynamic efficiency can be further optimised by adapting morphing strategies according to current flight condition, i.e., by moving the location of the maximum camber increment along the aerofoil chord. Furthermore, the pitching moment can be controlled independently from C_L and with little drag penalty; this is achieved by adapting different morphing strategies.

REFERENCES

1. KOTA, S., OSBORNE, R. F., JR., ERVIN, G., MARIC, D., FLICK, P. and PAUL, D. Mission adaptive compliant wing-design, fabrication and flight test. *RTO Applied Vehicle Technology Panel (AVT) Symposium*, RTO MP-AVT-168, Evora, Portugal, 20-24 April 2009.

https://doi.org/10.1017/aer.2016.113 Published online by Cambridge University Press

2. BARBARINO, S., BILGEN, O., AJAJ, R.M., FRISWELL, M.I. and INMAN, D.J. A review of morphing aircraft. *J Intelligent Material Systems and Structures*, August 2011, **22**, (9), pp 823-877.
3. THILL, C., ETCHES, J., BOND, I., POTTER, K. and WEAVER, P. Morphing skins. *Aeronautical J*, March 2008, **112**, (1129), pp 117-139.
4. CAMPANILE, L.F. and SACHAU, D. The belt-rib concept: A structronic approach to variable camber. *J Intelligent Material Systems and Structures*, March 2000, **11**, (3), pp 215-224.
5. CAMPANILE, L.F. and ANDERS, S. Aerodynamic and aeroelastic amplification in adaptive belt-rib airfoils. *Aerospace Science and Technology*, January 2005, **9**, (1), pp 55-63.
6. KOTA, S., HETRICK, J.A., OSBORN, R., PAUL, D., PENDLETON, E., FLICK, P. et al. Design and application of compliant mechanisms for morphing aircraft structures. *Proceedings of SPIE Smart Structures and Materials*, August 2003, **5054**, pp 24-33.
7. WOODS, B.K., BILGEN, O. and FRISWELL, M.I. Wind tunnel testing of the fish bone active camber morphing concept. *J Intelligent Material Systems and Structures*, April 2014, **25**, (7), pp 772-785.
8. SCHROEDER, T.A. and WAYMAN, C.M. The two-way shape memory effect and other "training" phenomena in Cu-Zn single crystals. *Scripta Metallurgica*, March 1977, **11**, (3), pp 225-230.
9. TREASE, B. and KOTA, S. Design of adaptive and controllable compliant systems with embedded actuators and sensors. *J Mech Design*, October 2009, **131**, (11), p 111001.
10. REDINIOTIS, O.K., WILSON, L.N., LAGOUDAS, D.C. and KHAN, M.M. Development of a shape-memory-alloy actuated biomimetic hydrofoil. *J Intelligent Materials Systems and Structures*, January 2002, **13**, (1), pp 35-49.
11. GEORGES, T., BRAILOVSKI, V., MORELLON, E., COUTU, D. and TERRIAULT, P. Design of shape memory alloy actuators for morphing laminar wing with flexible extrados. *J Mech Design*, September 2009, **131**, (9), p 091006.
12. KOREANSCHI, A., GABOR, O.Ş., AYRAULT, T., BOTEZ, R.M., MAMOU, M. and MEBARKI, Y. Numerical optimization and experimental testing of a morphing wing with aileron system, 24th AIAA/AHS Adaptive Structures Conference, 2016, p 1083.
13. GABOR, O.Ş., KOREANSCHI, A., BOTEZ, R.M., MAMOU, M. and MEBARKI, Y. Numerical simulation and wind tunnel tests investigation and validation of a morphing wing-tip demonstrator aerodynamic performance. *Aerospace Science and Technology*, June 2016, **53**, pp 136-153.
14. GABOR, O.S., KOREANSCHI, A. and BOTEZ, R.M. Optimization of an unmanned aerial system'wing using a flexible skin morphing wing. *SAE Int J Aerospace*, September 2013, **6**, (2013-01-2095), pp 115-1121.
15. GABOR, O.S., SIMON, A., KOREANSCHI, A. and BOTEZ, R.M. Aerodynamic performance improvement of the UAS-S4 Éhecatl morphing airfoil using novel optimization techniques. *Proceedings of the Institution of Mech Engineers, Part G: J Aerospace Engineering*, June 2016, **230**, (7), pp 1164-1180.
16. GABOR, O.Ş., SIMON, A., KOREANSCHI, A. and BOTEZ, R.M. Improving the UAS-S4 Éhecal airfoil high angles-of-attack performance characteristics using a morphing wing approach. *Proceedings of the Institution of Mechanical Engineers, Part G: J Aerospace Engineering*, Jan 2016, **230**, (1), pp 118-131.
17. SMITH, R.C. *Smart Material Systems: Model Development*, 2005, Society for Industrial and Applied Mathematics, Philadelphia, Pennsylvania, US.
18. LOCKYER, A.J., MARCHTIN, C.A., LINDNER, D.K., WALIA, P.S. and Carpenter, B.F. Power systems and requirements for integration of smart structures into aircraft. *J Intelligent Materials Systems and Structures*, April 2004, **15**, (4), pp 305-315.
19. TIECK, R.M., MOHANCHANDRA, K.P. and CARMAN, G.P. Smart material actuators for airfoil morphing applications. *Proceedings of SPIE Smart Structures and Materials*, July 2004, **5390**, pp 235-246.
20. BARTLEY-CHO, J.D., WANG, D.P., MARCHTIN, C.A., KUDVA, J.N. and WEST, M.N. Development of high-rate, adaptive trailing edge control surface for the smart wing phase 2 wind tunnel model. *J Intelligent Materials Systems and Structures*, April 2004, **15**, (4), pp 279-291.
21. JACOBS, E. N. Airfoil Section Characteristics as Affected by Protuberances, NACA Report No. 446, 1932.
22. MACK, S., BREHM, C., HEINE, B., KURZ, A. and FASEL, H.F. Experimental investigation of separation and separation control on a laminar airfoil, 4th AIAA Flow Control Conference, June 2008, pp 23-26.

https://doi.org/10.1017/aer.2016.113 Published online by Cambridge University Press

23. GROSS, A. and FASEL, H.F. Numerical investigation of separation for airfoils at low Reynolds numbers, 40th Fluid Dynamics Conference and Exhibit, June 2010, p 4736.
24. KOREANSCHI, A., SUGAR-GABOR, O. and BOTEZ, R.M., Numerical and experimental validation of a morphed wing geometry using Price-Païdoussis wind tunnel testing. *Aeronautical J*, May 2016, **120**, (1227), pp. 757-795.
25. GIGUERE, P. and SELIG, M.S. Freestream velocity corrections for two-dimensional testing with splitter plates. *AIAA J*, July 1997, **35**, (7), pp 1195-1200.
26. PANKHURST, R.C. and HOLDER, D.W. *Wind-Tunnel Technique: An Account of Experimental Methods in Low- and High-Speed Wind Tunnels*. 1952, Pitman. Bath, England.
27. ABBOTT, I.H., VON DOENHOFF, A.E. and STIVERS, L.S. Summary of airfoil data. National Advisory Commitee for Aeronautics. Report, 1945.
28. WOLKEN-MÖHLMANN, G., KNEBEL, P., BARTH, S. and PEINKE, J. Dynamic lift measurements on a FX79W151A airfoil via pressure distribution on the wind tunnel walls. *J Physics: Conference Series*, July 2007, **75**, (1), p 1.

https://doi.org/10.1017/aer.2016.113 Published online by Cambridge University Press